3D printed rotor blades for a research wind turbine: Aerodynamic and structural design and testing

3D printed rotor blades for a research wind turbine: Aerodynamic and structural design and testing

J Alber[1,3], L Assfalg[1,6], C N Nayeri[1], C O Paschereit[1], M Lahr[2], L Semmler[3], J Twele[3], J Fortmann[3], J Fischer[4], K Latoufis[5], I Dorn[6]

[1] Technische Universität (TU) Berlin, Hermann-Föttinger Institut (HFI), Müller-Breslau-Str. 8, 10623 Berlin
[2] Technische Hochschule (TH) Wildau, Hochschulring 1, 15745 Wildau, Germany.
[3] Hochschule für Technik und Wirtschaft (HTW) Berlin, Wilhelminenhofstr. 75A, 12459 Berlin, Germany
[4] SMART BLADE GmbH, Waldemarstr. 39, 10999 Berlin, Germany
[5] School of Mechanical Engineering, National Technical University of Athens (NTUA), Iroon Politechniou 9, Zografou 15772, Athens, Greece
[6] ERNI e.V., Tannenheckerweg 5, 34127 Kassel, Germany

Author contact email: joerg.alber@posteo.de

Keywords: Small rotor blades, 3D printing, Gyroid, PLA, FDM, Wind tunnel tests

Abstract. This study combines the design, the 3D printing and the testing of a small 3-bladed wind turbine rotor for research and teaching purposes. The objective is the additive manufacturing of a rotor with a radius of one meter, as an alternative to subtractive methods, such as computerized milling. The blade design is developed using freely available software packages. The aerodynamic considerations include the airfoil selection, the calculation of the blade geometry and the simulation of the ultimate load cases. The structural considerations are focussed on the printable materials, the infill structures and the retrofit of a load-carrying spar. The rotor blades are 3D printed with the BigRep One at the maker space of the TH Wildau. The structural integrity of the prototype blade is tested in terms of the ultimate root bending moments and the centrifugal forces at the HTW Berlin. The aerodynamic run-up tests are performed at the large wind tunnel of the TU Berlin measuring the power curves. The successful prototype paves the way for follow-up projects, such as open field tests and the 3D printing of larger rotor blades.

1. Introduction

Additive manufacturing is a sunrise industry and 3D printing technologies are an innovation driver in most scientific disciplines. The bandwidth of applications reaches from precision engineering, for instance human prothesis and robotics to large constructions, such as entire residential buildings [1]. In addition, the research on 3D printing methods is often based on open access principles, i.e. the free sharing of ideas and blueprints. In aerodynamics, lightweight applications include the wings of small air vehicles [2,3] and the rotor blades of wind turbines [4]. In general, aerodynamic bodies are exposed to a complex combination of steady and unsteady loads. Rotor blades, in particular, need to resist fluctuating bending forces, countless load cycles due to the blade rotation and the intermittent effects of inflow turbulence, wind shear and (local) stall [5,6].

Figure 1. (a) Rotor blade design and the load carrying spar. (b) 3D Printed blade during wind tunnel tests.

Hence, a wide range of both aerodynamic and structural requirements need to be fulfilled by 3D printed rotor blades, see Figure 1b. This paper merges the outcome of several low budget research projects over the past four years [7,8]. After this introduction, section 2 describes the aerodynamic design, i.e. the airfoil selection, the blade geometry and the simulation of the maximum structural loads. In section 3, different materials and infill structures are investigated in order to determine the structural blade design. The 3D printing process and the stress tests validating the strutural integrity of the blades are presented in section 4. Section 5 summarizes the run-up tests in the wind tunnel followed by the concluding section 6. In general, the terms *printing* and *3D printing* are used synonymously and *rotor blades* refer to small horizontal axis wind turbines (SHAWTs).

2. Aerodynamic considerations

The blade design, see Figure 1a, is preconditioned by the wind tunnel facility and the available 3D printer. The rated inflow velocity is u = 7.5 ms^{-1} and the rotor radius is restricted by the maximum printing volume, R = 1 m. For security purposes, the rotational speed is limited to $n_{max} \approx$ 800 min^{-1} leading to a design tip speed ratio (TSR) of λ_d = 4 at a Reynolds number of $Re \approx 1 \cdot 10^5$. Furthermore, the blade design is based on one identical airfoil from root to tip.

2.1 Airfoil selection

Low speed airfoils are characterized by a beneficial performance at $Re < 5 \cdot 10^5$ compared to high speed airfoils of multi-MW wind turbines, which operate at $Re >> 1 \cdot 10^6$. Usually, at $Re > 2 \cdot 10^5$, the laminar-to-turbulent transition of the boundary layer (BL) occurs gradually within a certain transition region along the airfoil chord. However, at $Re < 2 \cdot 10^5$ the BL tends to stagnate prematurely generating the so-called laminar separation bubble on the suction side, especially at low AoA [9]. Even if the flow reattaches in the form of a turbulent BL, the aerodynamic efficiency drops drastically, see Figure 2c. This unsteady process cannot be predicted by low-fidelity simulation codes, such as XFOIL. Hence, several low speed airfoils for use on small rotor blades are evaluated at $Re \approx 1 \cdot 10^5$ adopting the wind tunnel data from [10,11]. The airfoil selection matrix combines both structural and aerodynamic aspects, which are equally weighted, as summarized in Table 1.

Table 1. Airfoil selection parameters.

Parameter	Weight	Reason
Maximum thickness	50.0 %	Stability of rotor blade
Aerodynamic efficiency	12.5 %	Maximum lift-to-drag ratio and power output
High lift performance	12.5 %	Slender blade design and low weight
Stall behaviour	12.5 %	Reduced dynamic loads and improved power output
Sensitivity to surface roughness	12.5 %	Idem (printed surface is relatively rough)

According to Table 1, the preferred airfoils are found to be in the following order (maximum thickness given in brackets): 1. FX63-137 (13.7 %c), 2. SD7062 (14 %c), and 3. Clark-Y (11.7 %c). The remainder of this report refers to the FX63-137, which was developed in the 1980s by Wortmann at the Institut für Aerodynamik und Gasdynamik (IAG) of the Stuttgart University. Originally intended for use on wings of small airplanes, it has become popular as a low speed airfoil, especially considering surface roughness effects [12]. More recently, several studies have emphasized its suitability for use on SHAWTs [10,13].

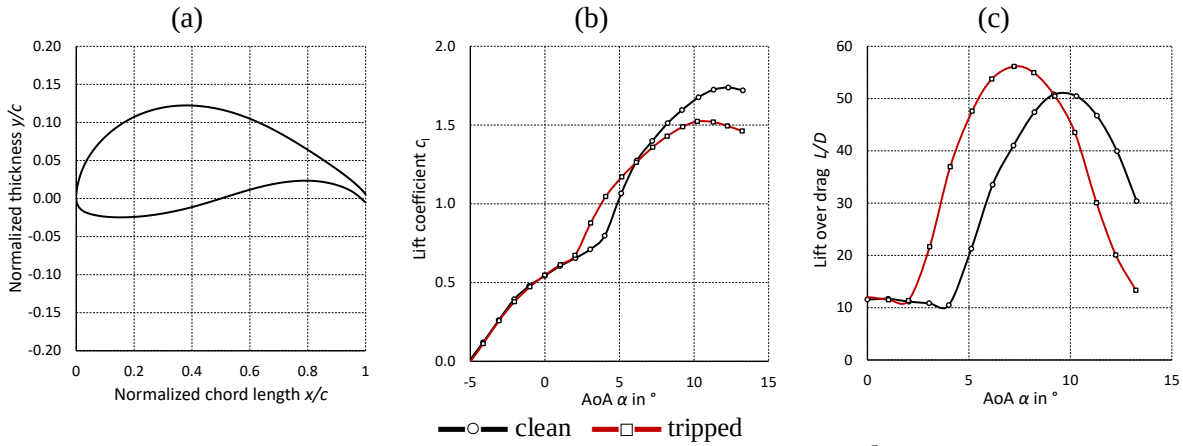

Figure 2. Experimental data of FX63-174. Clean and tripped cases at $Re = 1 \cdot 10^5$. (a) Airfoil coordinates. (b) Lift coefficients (c) Lift over drag.

Figure 2a illustrates the airfoil coordinates and Figure 2b and c the polar data of the FX63-137 in both the clean and the tripped cases, as published by [10]. In the tripped case, forced leading edge transition is triggered by Zig Zag (ZZ) turbulator tape in order to emulate surface roughness effects, which are crucial to modern blade design. The height of the ZZ tape is h_{ZZ} = 0.11 %c and it is attached on both the suction side and the pressure side at a chordwise position of x_s = 5 %c and x_p = 2 %c, respectively. At $Re \approx 1 \cdot 10^5$, the tripped case generates similar lift, and improved drag coefficients, so that L/D (α) is improved. The reason is that the BL transition is initiated close to the leading edge due to the ZZ tape, as such eliminating the separation bubble already at $\alpha \approx 2°$ rather than at $\alpha \approx 4°$, see Figure 2c. At higher angles of attack (AoA), 5° < α < 10°, the airfoil performance is similar comparing the clean case, L/D_{max} = 50 at α_d = 9°, to the tripped case, L/D_{max} = 55 at α_d = 7.5°. Hence, in both cases, the design lift coefficients are relatively high, c_l (α_d) ≈ 1.5, see Figure 2b, leading to a slender blade design.

2.2. Aerodynamic blade design and simulation

The blade geometry, i.e. the chord length c (r) and the twist angle θ (r), is determined by means of the aerodynamic blade optimization procedure of Betz and Schmitz (1956), as described by [5]. The Schmitz design is implemented in the simulation software QBlade [14] based on the following equations,

$$\lambda(r) = 2\pi n r (60u)^{-1}, \quad (1)$$

where n is the rotational speed in min^{-1} and r the local rotor radius in m,

$$c(r) = 16\pi r [B \cdot c_l(\alpha_d)]^{-1} \sin^2\{3^{-1} tan^{-1}[R \cdot (\lambda_d \cdot r)^{-1}]\}, \quad (2)$$

where B is the number of blades and $\lambda_d = \lambda(R)$,

$$\theta(r) = \varphi(r) - \alpha_d(r) = (2/3) \cdot \tan^{-1}[R \cdot (\lambda_d \cdot r)^{-1}] - \alpha_d(r), \quad (3)$$

where φ (r) is the inflow angle in °.

The blade geometry refers to the clean airfoil performance, c_l (α_d), the total rotor radius, R = 1 m, and the design TSR, λ_d = 4. In this way, c (r) and θ (r) are computed at 46 blade sections, expressed in %R. According to Figure 3a, the effective blade length is 90.7 %R = 0.907 m. Between 12.3 %R < r < 19.3 %R, the root cylinder merges into the first airfoil section, where the maximum chord length and twist angle is c (r) = 18.2 %R and θ (r) = 25.7°. Subsequently, c (r) and θ (r) decrease steadily until the tip section. The blade performance is simulated using the Blade Element Momentum (BEM) module of QBlade based on the iteration loop formulated by [6]. Note that the simulation results depend on the quality of the imported airfoil polar data. Furthermore, empirical correction algorithms are activated including root and tip losses, thrust forces of heavily loaded rotors (Glauert correction) and spanwise crossflow effects. Apart from that, all pitch and rotational speed controllers are deactivated. According to the wind tunnel conditions, two steady inflow velocities are considered, u = 5 ms^{-1} and u = 7.5 ms^{-1}.

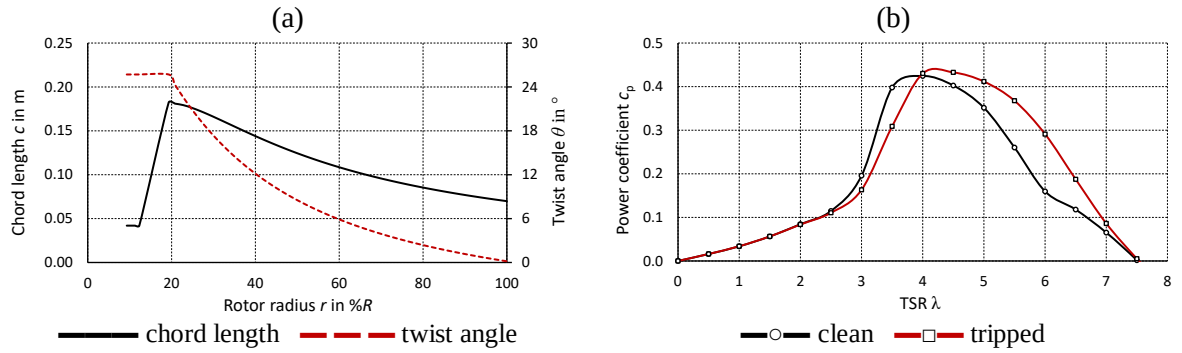

Figure 3. (a) Blade geometry, chord length and twist angles over rotor radius. (b) Characteristic power curves.

At λ_d, the Reynolds number along the blade length is in the order of $Re \approx 0.9 \cdot 10^5$ and $Re \approx 1.3 \cdot 10^5$, respectively. Figure 3b shows the characteristic power curves, where $c_{p,max} = 0.42$ in the clean, and $c_{p,max} = 0.43$ in the tripped case. Regarding the structural loads, the maximum rotational speed is reached at $n_{max} = 600$ min^{-1}, where $\lambda_{max} \approx 8$. At rated inflow, the root bending moment reaches $M_{max} = 30$ Nm and the corresponding centrifugal force amounts to $F_{max} = 1850$ N. Note that F_{max} is a crucial design load of SHAWTs, as it is proportional to n^2. Applying a security factor of almost 2, the ultimate load cases (ULCs) in the wind tunnel are defined as $M_{ulc} = 60$ Nm and $F_{ulc} = 3000$ N. Moreover, the mechanical brake is activated at n_{max} stopping the rotor after each run-up test, see section 5.1. For safety purposes, M_{ulc} is therefore considered in both the out-of-plane and the in-plane direction. Note that the industry standard *IEC 61400-2: Part 2: Small wind turbines* is not applied, since the prescribed ULCs refer to open field conditions and a service time of various years rather than temporary wind tunnel testing.

3. Structural considerations

The BigRep PRO contains a printing volume of up to 1 m^3 restricting the rotor radius to $R = 1$ m. The blades are printed in one piece by means of fused filament modelling (FDM). The structural design is based on both the material study and the investigation of different infill structures.

3.1 Material study

The FDM or fused filament fabrication (FFF) is a material extrusion process [15]. The filament is melted inside the heated nozzle, which moves rapidly in space printing the object layer by layer. In this way, a wide range of pure, modified or enhanced thermoplastic or elastomer polymers is processed, such as ABS (Acrylonitrile Butadiene Styrene), PTEG (Polyethylene Terephthalat) and PLA (Polyactic Acid). The focus is on PLA-based materials due to the wide range of applications and the comprehensive amount of literature data. In addition, PLA is considered to be biodegradable, non-toxic and CO_2 neutral, i.e. a feasible alternative to petrochemical-based polymers [16]. In cooperation with BigRep GmbH, the following PLA-based filaments are investigated: 1. Pro-HT ($T_v = 115$ °C), 2. Hi-Temp ($T_v = 160$ °C), and 3. PLA ($T_v = 60$ °C). Compared to standard PLA, Pro-HT and Hi-Temp are characterized by the relatively high Vicat softening temperature, T_v (given in brackets), at which point the material loses its properties. The manufacturer's specifications are limited to single characteristic values, most importantly the elasticity modulus and the ultimate tensile strength [17]. Furthermore, the data sheets only refer to the so-called vertical printing direction, whereby the object is extruded in parallel to the printing bed. However, in the current case, the blades are printed in the horizontal direction, i.e. the upright position, as illustrated in Figure 4a. Hence, according to the DIN ISO 527-2/1A, independent tensile tests are performed using the ZMART PRO universal testing machine at the HTW Berlin. A total of 24 standard probes is tested, i.e. 4 identical probes of each material and in both printing directions. The printing parameters, such as the layer height of 0.5 mm, refer to empirical values, as discussed in section 4.1. Besides, [18] show that the maximum tensile strength of PLA is reached, if the ratio between nozzle diameter and layer height is greater than 1.6. In the current case, this ratio is 2.

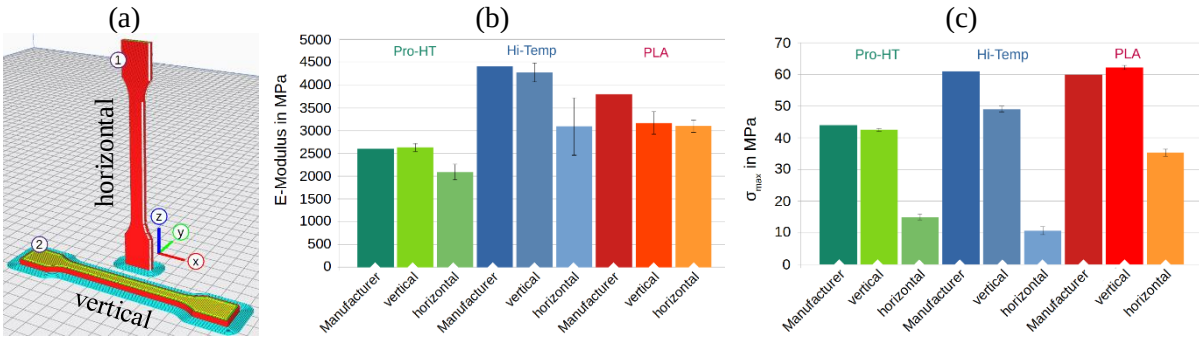

Figure 4. Tensile tests. (a) Probes and printing directions. (b) Elasticity modulus. (c) Ultimate tensile strength.

Figure 4b shows that, in the vertical printing direction, the elasticity modulus, E, is similar to the specifications given by the manufacturer [17]. However, in the horizontal direction (upright position), E is decreased in case of all tested materials. This tendency is significantly more pronounced regarding the ultimate tensile strength, σ_{max}, as shown in Figure 4c. The reason is that, in the horizontal position, E and σ_{max} are determined by the interlayer bonding, i.e. the soldering between the layers. The weak link between the printed layers leads to the drop in stiffness and strength [18]. As such, the type of fracture is smooth in the horizontal and frayed (irregular) in the vertical case [8]. For all tested probes, the stress and strain curves are typical for thermoplastics without yield point.

3.2 Structural blade design

According to the results summarized in Figure 4b and c, PLA-based materials do not meet the structural requirements of the current rotor blade. Even if printed as one solid body, i.e. assuming up to 3 times the printing duration and the weight, the blade would still not fulfil the ULCs, as calculated in section 2.2. Therefore, the blade shell is reinforced by a load-carrying spar made of carbon fiber reinforced plastics (CFRP). The spar consists of 8 prefabricated tubes that are assembled in a telescopic configuration relative to the maximum thickness of each blade section, as shown in Figure 1a. All the tubes are interlocked forming one solid root section with an outer diameter of 20mm, which narrows down to an outer diameter of 5 mm close to the tip, see Figure 6c and d. The tapered drill hole for retrofitting the modular spar is part of the printed structure, see Figure 5. The protruding root part is clamped to the hub by means of an additional aluminum mount. As such, the shell is structurally decoupled from the load-carrying spar, see Figure 6e. The complete assembly is glued together with epoxy resin. According to the material specifications of [19], the CFPR tubes are characterized by E = 98·10^3 MPa and σ_{max} = 1280 MPa, thus exceeding both the material properties of PLA by approximately 30 times. The simplified design stress calculation at the blade root is,

$$\sigma_d = \left(M_{ulc,x}^2 + M_{ulc,y}^2\right)^{0.5} \cdot W^{-1} = 108\ MPa, \quad (4)$$

where $M_{ulc,y}$ = 60 Nm is the out-of-plane, $M_{ulc,x}$ = 60 Nm the in-plane root bending moment and W the cylindrical section modulus in mm^3. Hence, at the root, the maximum tensile strength of the reinforcing spar, σ_{max}, exceeds σ_d by more than 10 times. Next, different interior structures are investigated in order to transfer the aerodynamic load distribution efficiently from the shell to the spar and all the way to the hub. The slicing software Ultimaker Cura is used to implement a variety of infill patterns, e.g. triangular, grid or cubic [2]. The gyroid was discovered in 1970 by NASA researcher Schoen [20]. It is part of the triply-periodic minimal surfaces resulting in a twisted wave structure that looks similar to honeycomb configurations [21]. Conventional manufacturing methods, such as moulding or milling, are not viable for implementing complex and mostly hollow lattice structures from within the object, see Figure 5. Hence, several studies demonstrate the benefits of gyroid infills using additive methods [22]. Applying a special graphene lattice configuration, the resulting gyroid cubes are characterized by extraordinary stability at very low density, i.e. the main requirements of lightweight applications [23,24].

Figure 5. Blade cross section including spar hole and gyroid infill, looking from tip to root. (a) Cura design. (b) 3D printed prototype blade including residues.

In terms of FDM methods, both the duration and the printing quality is beneficial due to its smooth and continuous pattern reducing mechanical vibrations of abrupt nozzle movements (rattling) compared to e.g. cross or honeycomb infills. However, several PLA-based experiments report that gyroid infills lead to reduced stiffness, *E*, compared to the classic grid [2] or honeycomb infills [25]. Overall, the mentioned references agree in its isotropic properties making gyroid particularly attractive for applications that are exposed to varying load directions, such as rotor blades. It is implemented during the slicing process based on the original equations of [20] in the form of the trigonometric approximation [26],

$$\cos(x) \cdot \sin(y) + \cos(y) \cdot \sin(z) + \cos(z) \cdot \sin(x) = 0, \quad (5)$$

where *x*, *y*, *z* refer to the directions in space. Figure 5 shows the gyroid infill joining the aerodynamic shell and the spar hole.

4. Printing and structural testing

The printing process and the blade assembly is explained, followed by the static stress tests of the prototype blade.

4.1 Printing process

The printing file is generated by means of the following software packages, successively:

1. QBlade (v0.96): The mesh of the shell (.stl) is exported in high resolution (min. 200 *x* 2000).
2. FreeCAD (0.19.2): The mesh is imported for editing, in this case implementing the spar hole. Subsequently, defects in the mesh are analysed and repaired for improved printing quality using the adequate plugin or, alternatively, the software Autodesk Meshmixer (3.5).
3. Ultimaker Cura (4.11): The final mesh is imported and placed on the printing bed. The support structure (default) is created and the printing parameters are defined, including the infill structure. The blades are sliced and the machine code is generated (.gcode).

The project files are accessible in the multimedia section of this report. The interrelated printing parameters (given in brackets) determine both the performance and the quality of the resulting objects [15]. In relation to the selected material (Pro-HT), the crucial settings include the printing direction (upright position), the layer height (0.5 mm), the wall thickness (2 mm), the infill structure (gyroid) and the infill density (10 %). In addition, default values are used for temperature and speed. Pro-HT is selected due to its high temperature resistance and the advanced environmental compatibility [17]. The layer height is selected due to the recommendation of the TH Wildau engineers. The infill density is closely related to the wall thickness. In the current case, 2 mm and 10 % is considered to be a sound compromise between stability, weight and duration. Previous crash-tests of similar rotor blades (R = 0.55 m) at the HTW Berlin have shown that a gyroid infill density of 6.2 % combined with a wall thickness of 1.2mm is preferable over 21.5 % and 0.6 mm [7]. The duration is 10 h per blade, each processing 0.8 kg of filament. During the first attempt, two blades are finished successfully, however, the third one is printed erroneously, as displayed in Figure 6a. The support structure is depicted in Figure 6b, which is necessary for maintaining the blade in a stable upright position throughout the complete process. After removing it, the minor residues next to the root section are polished with fine grain sandpaper together with various additional irregularities alongside the entire trailing edge.

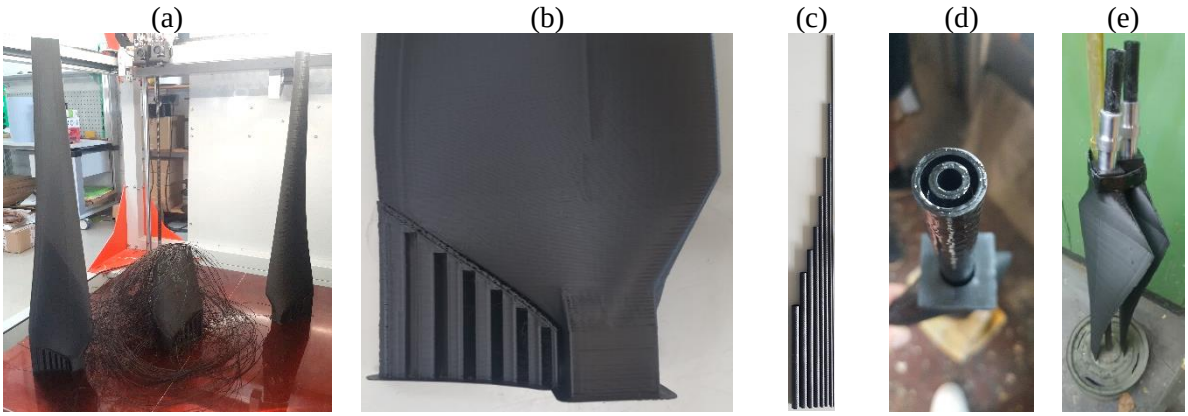

Figure 6. (a) Finished blades and printing error inside the BigRep PRO. (b) Support structure next to the root section. (c) Telescopic spar configuration. (d) Insertion and bonding of tubes from blade root. (e) Final assembly with aluminium mount.

The relatively rough surface is characterized by the riblets from the printed layers. However, additional surface treatments, such as coatings, are beyond the scope of this study. Note that the vertical printing direction is discarded, as it requires a more complicated support structure that would cover a large surface area of the blade. As a result, both the material volume and the duration would be approximately double. Moreover, the residues of the support structure would negatively affect both surfaces alongside the entire blade length, especially at the leading edge.

4.2 Blade assembly and stress tests

The blade assembly starts by roughening the surfaces of both the drill hole and the CFRP tubes using fine grain sandpaper. Before applying the epoxy resin, all surfaces are cleaned thoroughly with acetone. One by one, each tube is wetted with a relatively runny epoxy mixture and inserted from the root section into the blade, see Figure 6d. It is important that trapped air bubbles are released. Then, the aluminum mount is put over the root section using a more viscid epoxy mixture. The blade is then cured for 24 h in the upright position, see Figure 6e. Its final weight is 1.2 kg and the centre of gravity is at r = 39 %R.

Next, the prototype blade is exposed to the ULCs, again using the universal testing machine at HTW Berlin. Apart from overall safety considerations, the stress tests are focused on potential buckling damages and cracks inside the printed shell. Following [27], the ultimate root bending moments are tested by introducing a subsequent point forces at three blade positions and in both bending direction, as shown in Figure 7a and b. The ultimate centrifugal force, F_{max} = 3000 N, is applied via the pulling force of a heavy duty crane.

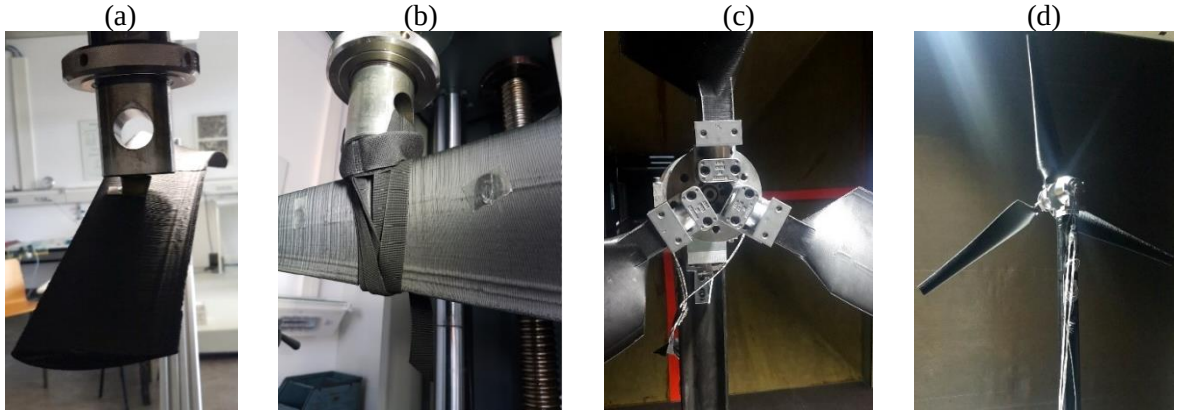

Figure 7. (a) Out of plane bending. (b) In plane bending. (c) Hub clamping. (d) Rotor during run-up tests.

Table 2. Root bending moments and tip deflection

	Out of plane			**In plane**		
Blade length or lever arm [mm]	490	690	840	570	690	840
Deflection at tip [mm]	29	78	107	40	40	27
Root bending moment [Nm]	102	103	68	83	85	40

Table 2 summarizes both bending moments at each point along the blade length, in most cases exceeding M_{ulc} = 60 Nm. At the position close to the tip (highest lever arm), the maximum deflection is reached, as permitted by the test bed. After several stress tests, the printed shell is fully intact without showing any cracks or signs of buckling. Furthermore, the reinforced blade returns back to the (unloaded) zero position without any permanent deflections. Please note that fatigue tests are out of the scope of this study.

5. Wind tunnel tests

5.1 Experimental setup

The large close-loop wind tunnel at the HFI of the TU Berlin accommodates several research wind turbines. The area of the low speed test section is 4.2 m *x* 4.2 m at a rated inflow velocity of u = 7.5 ms^{-1}. A detailed description of the wind tunnel facility is provided by [28]. In the current case, the blockage ratio between the area of the test section and the rotor is approximately 18 %. Exceeding a blockage ratio of 10 %, the rotor performance is significantly affected by the wind tunnel walls [29], as further discussed in section 5.2. The set-up consist of the tower, which is placed in the center of the test section, and the rotor, which is attached directly to the spinning shaft. The mechanical brake is activated by a stepping motor in order to bring the rotor to standstill either smoothly or abruptly. The shaft is equipped with an incremental encoder measuring the rotational speed. Data is recorded by means of an Arduino (UNO) system at a sampling rate of 10 Hz. Prior to the run-up tests, the moment of inertia is derived experimentally by releasing predefined weights from a flywheel, which is attached to the final rotor assembly. The inflow velocities are measured via two parallel Prandtl tubes that are connected to a separate differential pressure sensor. Parallel to that, the temperature and the ambient pressure is captured. The measurements are conducted at different constant inflow velocities, u = [4.9, 6.2, 7.5] ms^{-1}. The turbulence intensity of the inflow field is below 1 % and the duration of each run-up test is approximately 30 s. Phython (3.7) is used for post-processing the rotor power in W,

$$P_r = M_r\omega = I\omega dt(2\pi n/60), \tag{6}$$

where M_r is the rotor torque in Nm, ωdt the angular acceleration in s^{-2} and I = 0.863 kg·m^2 the constant moment of inertia. The dimensionless power coefficient, c_p, is the ratio between P_r and the power of the inflow field. Moreover, no wind tunnel blockage correction is applied.

5.2 Experimental results

Figure 8a shows that, depending on the inflow velocity, maximum power is reached at $P_{r,max}$ = [64, 124, 216] W, respectively. In all cases, the maximum power coefficient is $c_{p,max}$ = 0.3 (± 0.01), see Figure 8b. Compared to the design TSR, λ_d = 4, see section 2.2, the optimum TSR of the experiments is increased significantly to λ_{opt} = 5.4 (± 0.1). As a result, c_p (λ_d) drops to 0.23. The reason for the TSR shift is that the blade design is based on free flow rather than wind tunnel conditions. According to the BEM simulations, the deceleration of the wake flow is described by the axial induction factor, a. At the optimum value, a (λ_d) = 1/3, $c_{p,max}$ is reached. However, the wind tunnel blockage leads to elevated axial wake velocities, so that the effective a (λ_d) < 1/3, as previously reported by [28]. In general, the axial induction is increased for higher TSR. Hence, inside the wind tunnel, $c_{p,max}$ is reached at λ_{opt} = 5.4, where both the axial induction factor and the resulting AoA are closer to the design values of a = 1/3 and α_d = 9°, respectively. These results are in close agreement with wind tunnel experiments based on similar rotor blades, i.e. the FX63-174, R = 1.1 m and a blockage ratio of 21 %. As such, [13] report that the design TSR is shifted from λ_d = 5 to $\lambda_{opt} \geq 8$ due to the wind tunnel effects reaching $c_{p,max} \leq 0.37$.

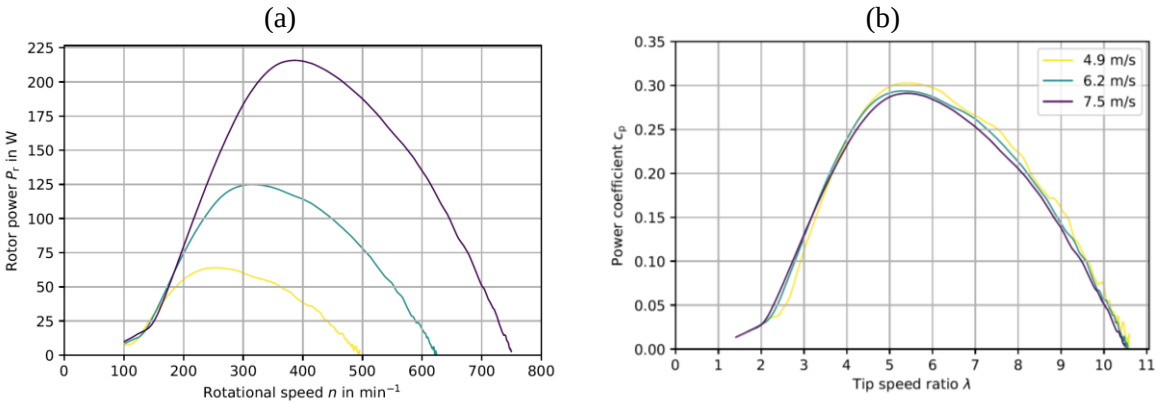

Figure 8. Run-up wind tunnel tests (a) Power over rotational speed. (b) Power coefficient over tip speed ratio.

In summary, the current rotor is running successfully. However, the power curve is off-design due to the wind tunnel wall effects, which are disregarded during the BEM-based blade design process. After numerous run-up tests, the 3D printed rotor blades remain fully intact, without showing any cracks or signs of buckling damage.

6. Conclusions

This study combines the design, the 3D printing and the testing of a small wind turbine rotor for research and teaching purposes. The main conclusions are summarized in terms of the following criteria. The overall progress estimation from the authors is given in brackets in %.

Precision (70 %). The shape of the blades appears to be precise. However, the accurate verification of their geometry is pending. The surface is characterized by riblets, which result from the layer by layer printing. The trailing edge is bulky and needs polishing with fine grain sandpaper. The complex gyroid infill structure is implemented successfully.
Stability (100 %). The ultimate load cases are applied by means of static stress tests. The shell is fully intact, so that the load transfer via the gyroid infill is considered to be successful. For use in the open field, the ultimate load cases need to be calculated in accordance with the *IEC 61400-2*. Furthermore, PLA-based materials require an additional protective surface treatment to prevent blade erosion due to rough weather conditions.
Environment (30 %). The Pro-HT filament is biodegradable and CO_2 neutral. However, the necessity for retrofitting a CFRP spar plus epoxy resin partly defeats this point.
Efficiency (80 %). Given the access to a large printer, the process is efficient. A set of blades is fabricated and assembled within less than a week. In general, PLA-based filament is cheap and readily available. Printing errors should be accounted for in the planning.
Open access (100 %). The blade design is entirely based on freely available software packages. The project files are accessible in the multimedia section of this report or by contacting the authors.
Functionality (70 %). According to the wind tunnel measurements and compared to literature data, the rotor performs satisfactorily. Further tests are required to evaluate the power curves, which are significantly influenced by the blockage effects due to the wind tunnel walls.
Outlook. The current setup is already in use for research and teaching purposes at the participating entities. Next steps will focus on both fatigue loading and open field tests. Future blade designs might include the development of innovative airfoils, flow control devices (e.g. Gurney flaps and trailing edge flaps), advanced materials, such as carbon fiber reinforced filaments and optimized infill structures. In this way, the 3D printing of larger rotor blades might become feasible in the near future.

References

[1] Tofail S A M, Koumoulos E P, Bandyopadhyay A, Bose S, O'Donoghue L and Charitidis C 2018 Additive manufacturing: scientific and technological challenges, market uptake and opportunities *Materials Today* **21** 22-37
[2] Pecho P, Ažaltovič V, Kandera B and Bugaj M 2019 Introduction study of design and layout of UAVs 3D printed wings in relation to optimal lightweight and load distribution *Transp. Research Proc.* **40** 861-68
[3] Moon S K, Tan Y E, Hwang J. and Yoon Y J 2014 Application of 3D Printing Technology for Designing Light-weight Unmanned Aerial Vehicle Wing Structures *Int. J. of Precis. Eng. and Manuf.-Green Tech*. **1** 223–28
[4] Strauss K 2012 https://www.ge.com/news/reports/tipping-point-3d-printed-blade-parts-can-help-take-wind-power-to-the-next-level (last access 28 March 2022)
[5] Gasch R and Twele J 2012 *Wind Power Plants - Fundamentals, Design, Construction and Operation* Berlin Heidelberg: Springer Ed. 2
[6] Hansen M O L 2015 *Aerodynamics of Wind Turbines* London: Earthscan from Routledge Ed.3
[7] Semmler L 2018 *Untersuchung zur Fertigung von Kleinwindrad-Flügeln mittels 3D-Druck* BA Thesis Hochschule für Technik und Wirtschaft Berlin Germany
[8] Assfalg L 2021 *Printing rotor blades for a small wind turbine* MA Thesis Technische UniversitätBerlin Germany
[9] Bastedo W G and Mueller T J 1986 Spanwise Variation of Laminar Separation Bubbles on Wings at Low Reynolds Numbers *Journal of Aircraft* **23** 687-94
[10] Selig M and McGranahan B D 2004 *Wind Tunnel Aerodynamic Tests of Six Airfoils for Use on Small Wind Turbines* NREL/SR-500-34515
[11] Lyon C A, Broeren A P, Giguère P, Gopalarathnam A and Selig M S 1998 *Summary of Low-Speed Airfoil Data* Virginia Beach: SoarTech Publications Vol. 3
[12] Huber A F and Mueller T J 1987 The effect of trip wire roughness on the performance of the Wortmann FX 63-137 airfoil at low Reynolds numbers *Experiments in Fluids* **5** 263–72
[13] Refan M and Hangan H 2012 Aerodynamic Performance of a Small Horizontal Axis Wind Turbine *ASME. J. Sol. Energy Eng.* **134**
[14] Marten D, Wendler J, Pechlivanoglou G, Nayeri C N and Paschereit C O 2013 *Development and Application of a Simulation Tool for Vertical and Horizontal Axis Wind Turbines* Proceedings of the ASME Turbo Expo 2013 Vol. 8
[15] Cuan-Urquizo E, Barocio E, Tejada-Ortigoza V, Pipes R B, Rodriguez C A and Roman-Flores A 2019 Characterization of the Mechanical Properties of FFF Structures and Materials: A Review on the Experimental, Computational and Theoretical Approaches *Materials* **12**
[16] Farah S, Anderson D G and Langer R 2016 Physical and mechanical properties of PLA, and their functions in widespread applications — A comprehensive review *Advanced Drug Delivery Reviews* **107** 367-92
[17] https://bigrep.com/filaments/ (last access 28 March 2022)
[18] Kuznetsov V E, Solonin A N, Urzhumtsev O D, Schilling R and Tavitov A G 2018 Strength of PLA Components Fabricated with Fused Deposition Technology Using a Desktop 3D Printer as a Function of Geometrical Parameters of the Process *Polymers* **10**
[19] https://www.carbonscout-shop.de/Home-English.html (last access 28 March 2022)
[20] Schoen A H 1970 *Infinite periodic minimal surfaces without self-intersections* NASA Electronics Research Center Cambridge
[21] Schoen A H 2012 Reflections concerning triply-periodic minimal surfaces *Interface Focus* **2**, 658-68
[22] Gür Y 2020 *Mathematical Modelling and Additive Manufacturing of a Gyroid*. In: Machado J, Özdemir N and Baleanu, D (eds) *Mathematical Modelling and Optimization of Engineering Problems. Nonlinear Systems and Complexity*, Vol 30. Springer, Cham

[23] Chandler D L 2017 https://news.mit.edu/2017/3-d-graphene-strongest-lightest-materials-0106 (last access 28 March 2022)
[24] Qin Z, Jung G S, Kang M J, Buehler M J 2017 The mechanics and design of a lightweight three-dimensional graphene assembly *Science Advances* **3**
[25] Beloshenko V, Beygelzimer Y, Chishko V, Savchenko B, Sova N, Verbylo D, Voznyak A and Vozniak I 2021 Mechanical Properties of Flexible TPU-Based 3D Printed Lattice Structures: Role of Lattice Cut Direction and Architecture *Polymers* **13**
[26] Weyhaupt A G https://plus.maths.org/content/meet-gyroid (last access 28 March 2022)
[27] Bürkner F, Wingerde A, Busmann H G 2008 *Testing of rotor blades of wind turbines* Bremerhaven: Fraunhofer Center for Wind Energy and Maritime Engineering
[28] Alber J, Soto-Valle R, Manolesos M, Bartholomay S, Nayeri C N, Schoenlau M, Menzel C, Paschereit C O, Twele J and Fortmann J 2020 Aerodynamic effects of Gurney flaps on the rotor blades of a research wind turbine *Wind Energy Science* **5** 1645-62
[29] Klein A C, Bartholomay S, Marten D, Lutz T, Pechlivanoglou G, Nayeri C N, Paschereit C O and Kraemer E 2018 About the suitability of different numerical methods to reproduce model wind turbine measurements in a wind tunnel with a high blockage ratio *Wind Energy Science* **3** 439-60